

A fast model based on muffin-tin approximation to study charge transfer effects in time-dependent quantum transport simulations: doped Si-SiO₂ quantum-dot systems

I-Lin Ho^{1, a)}

*ChiMei Visual Technology Corporation, Tainan 741, Taiwan,
R.O.C.*

(Dated: 8 October 2018)

This research theoretically studies transient electron transports in heterojunctions of gold metals and silicon quantum dots by using the time-dependent non-equilibrium green function (TDNEGF) method. The studied quantum dots are Si-SiO₂ core-shell nanoparticles that are doped with phosphorus impurities for low-voltage applications. In order to quickly compute devices having more than a thousand atoms, we demonstrate an analytical algorithm based on muffin-tin approximation to solve the Poisson equation for transient variations of electron densities, and apply the wide-band limit approximation for contacts of electrodes. Numerical results are described and discussed herein.

PACS numbers: 73.63.Kv, 05.60.Gg, 85.65.+h

Keywords: quantum dot, time-dependent non-equilibrium green function, poisson equation

^{a)}Electronic mail: sunta.ho@msa.hinet.net

I. INTRODUCTION

Photoelectric bioengineering - the use of photoelectric semiconductors as functional entities in biological systems - is heralded as an alternative option for signaling communications between organisms and physical devices in future biomedicines. In particular, research on quantum dots¹ has already revealed a variety of biologically-oriented applications, e.g. drug discovery^{2,3}, disease detection^{4,5}, protein tracking^{6,7}, and intracellular reporting^{8,9}. A qualitative understanding of these complex processes has been accessed by perturbative electron-photon interactions associated with strong electron correlations¹⁰, but the quantitative agreement between the first-principles theory and experiments is still unsatisfactory from the perspective of the ground-state density functional theory (DFT)^{11,12}.

In recent years, the majority of studies for quantum-dot electronics have focused on the time-dependent density functional theory (TDDFT)¹³ that provides a more rigorous theoretical foundation¹⁴. The formalism may also be easily extended to cover the interaction of electrons with light or environments by the time-dependent non-equilibrium green function (TDNEGF) technique^{15,16}, e.g. for the photon-assisted transport and fluorescence of contacted atomic devices.

Several scenarios of open quantum systems implemented with TDDFT have so far been suggested, including the ring-topology of the electronic circuit^{17,18} and the approximately-isolated atomic device^{19,20}. This present work adopts more general set-ups to study systems composed of functional atomic devices and environmental clusters as shown in Figure 1. The device in the central region focuses on the Si-SiO₂ core-shell quantum dots that are doped with phosphorus impurities²¹ for low-voltage applications. The effect of the Au(111) electrodes in the side regions is exactly accounted for by properly defined self-energies. For both the Si-SiO₂ quantum dots and Au electrodes, the initial Kohn-Sham (KS) single-particle Hamiltonians and the overlap matrices for systems in equilibrium are constructed by using DFT calculations in SIESTA programs^{22,23}. Based on the holographic electron density theorem and Runge-Gross theorem, the time-dependent electron dynamics are then determined by solving equations of motion for the reduced density matrix in the device region with the TDNEGF technique^{16,24}.

Computations of realistic devices having more than one thousand atoms by TDNEGF, however, are numerically demanding, because the electron motion has to be fully resolved,

leading to time steps in the sub-fs range. To arrive at a computationally efficient but still predictive method, this work introduces the numerical technique of Chen and co-researchers¹⁶ for open systems driven by time dependent bias potentials. Moreover, to consider the transient change of the electron density under bias potentials, this work demonstrates a capacitive network model²⁵ for Poisson solution by using the muffin-tin approximation. Rather than the conventional numerical Poisson-equation solution using discretized spatial grids¹⁵, this model presents analytical Hartree potential solutions accounting for the effects of electron density variations.

II. TIME-DEPENDENT NON-EQUILIBRIUM GREEN FUNCTION FOR QUASI-ONE-DIMENSIONAL OPEN QUANTUM SYSTEMS

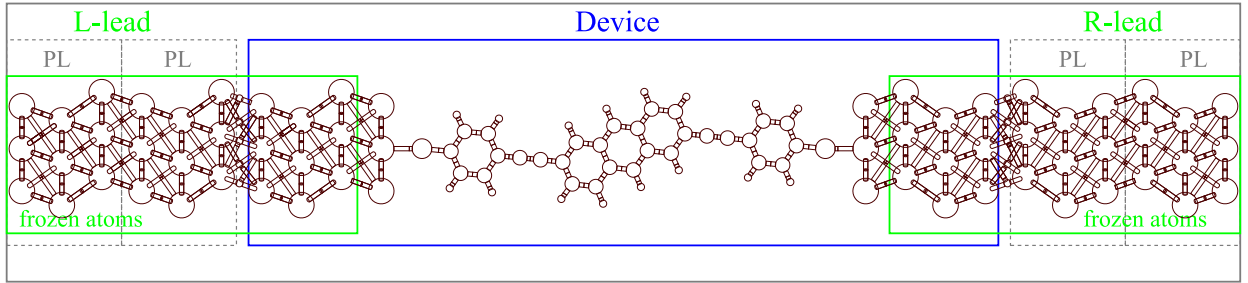


FIG. 1. Schematic representation of general simulation setups for open quantum systems including Au(111) electrodes and atomic devices.

Figure 1 shows regular open quantum systems, including Au(111) electrodes and atomistic devices. The systems is composed of several electronically-functional areas, partitioned as L-electrode (L), device (D), and R-electrode (R). The equation of motion (EOM) for electrons can be described by quantum dynamics:

$$i\dot{\sigma}(t) = [\mathbf{h}(t), \sigma(t)] \quad (1)$$

where $\mathbf{h}(t)$ is the Kohn-Sham Hamiltonian matrix, and the square bracket on the right-hand side (RHS) denotes a commutator. The matrix element of the single-electron density σ is defined by $\sigma_{ij}(t) = \langle a_j^\dagger(t)a_i(t) \rangle$, where $a_j^\dagger(t)$ and $a_i(t)$ are the creation and annihilation operators for atomic orbitals j and i at time t , respectively. On the basis of the atomic

orbital sets for electrons, the matrix representation of σ and \mathbf{h} can be written as

$$\mathbf{h} = \begin{bmatrix} \mathbf{h}_L & \mathbf{h}_{LD} & 0 \\ \mathbf{h}_{DL} & \mathbf{h}_D & \mathbf{h}_{DR} \\ 0 & \mathbf{h}_{RD} & \mathbf{h}_R \end{bmatrix}, \quad \sigma = \begin{bmatrix} \sigma_L & \sigma_{LD} & \sigma_{LR} \\ \sigma_{DL} & \sigma_D & \sigma_{DR} \\ \sigma_{RL} & \sigma_{RD} & \sigma_R \end{bmatrix} \quad (2)$$

Here, \mathbf{m}_L , \mathbf{m}_D , and \mathbf{m}_R ($\mathbf{m} \in \{\mathbf{h}, \sigma\}$) represent the matrix blocks corresponding to left-electrode L , device D , and right-electrode R partitions, respectively. Moreover, \mathbf{h}_{LR} and \mathbf{h}_{RL} are ignored due to the distant separation between L and R electrodes in common applications. It is noticed that the holographic electron density theorem and Runge-Gross theorem are adopted for time-dependent electron dynamics^{16,24}, stating that the initial ground-state density of the subsystem $\sigma_D(t_0)$ can determine all physical properties of systems at any time t . Hence \mathbf{h} and σ can be approximately expressed as functions of $\sigma_D(t)$ for a formally closed-form equation of motion as described below.

Placing Eq. (2) into Eq. (1), we can write the equation of motion for σ_D as

$$i\dot{\sigma}_{D,mn} = \sum_{\ell \in D} (h_{D,m\ell} \sigma_{D,\ell n} - \sigma_{D,m\ell} h_{D,\ell n}) - i \sum_{\alpha=L,R,N} Q_{\alpha,mn} \quad (3)$$

$$Q_{\alpha,mn} \equiv i \sum_{k_\alpha \in \alpha} (h_{D\alpha,mk_\alpha} \sigma_{\alpha D,k_\alpha n} - \sigma_{D\alpha,mk_\alpha} h_{\alpha D,k_\alpha n}) \quad (4)$$

Here, m and n denote the atomic orbital in partition D , k_α denotes the state of α ($\alpha=L, R$), and Q_α is the dissipation term due to the contacts with electrodes L and R . The transient current through an electrode's interfaces can be calculated by:

$$\begin{aligned} I_{\alpha \in \{L,R\}}(t) &= - \int_{\alpha} d\mathbf{r} \partial_t \rho(\mathbf{r}, t) = - \sum_{k_\alpha \in \alpha} \partial_t \sigma_{k_\alpha k_\alpha}(t) \\ &= i \sum_{k_\alpha \in \alpha} \sum_{\ell \in D} (h_{D\alpha,k_\alpha \ell} \sigma_{\alpha D,\ell k_\alpha} - \sigma_{D\alpha,k_\alpha \ell} h_{\alpha D,\ell k_\alpha}) \\ &= -tr[Q_\alpha(t)] \end{aligned} \quad (5)$$

A. Expressions of the dissipation function Q_α using the Green function formalism

To calculate the dissipation term Q_α in EOM and transient current equation, we use the time-dependent nonequilibrium Green's function (TDNEGF) formalism. We note that the overlap matrix is treated as an identity matrix when deriving Green function formalism in the

appendices. This replacement of the overlap-matrix by the identity matrix has been verified to be valid if the hamiltonian matrix is modified according to mathematical techniques in the textbook²⁶(Ch. 8.1.2). Appendix A describes the derivations and gives the formulae of Q_α :

$$Q_{\alpha,mn}(t) = - \sum_{\ell \in D} \int_{-\infty}^{\infty} d\tau \left[G_{D,m\ell}^<(t, \tau) \Sigma_{\alpha,\ell n}^A(\tau, t) + G_{D,m\ell}^R(t, \tau) \Sigma_{\alpha,\ell n}^<(\tau, t) + H.c. \right] \quad (6)$$

Here, the term associated with the complex-axis integral along the Keldysh contour γ_K (see Fig. 13) in Eq. (A34) is ignored. Green functions $\mathbf{G}^<$ and \mathbf{G}^R in Eq. (6) are calculated via Kadanoff-Baym equations^{16,27} as derived by Eqs. (A31) and (A32) in appendix A:

$$i \frac{d}{dt} \mathbf{G}_D^R(t, t') = \delta(t - t') + \mathbf{h}_D(t) \mathbf{G}_D^R + \Sigma^R \cdot \mathbf{G}_D^R \quad (7)$$

$$i \frac{d}{dt} \mathbf{G}_D^<(t, t') = [\Sigma^R \cdot \mathbf{G}^< + \Sigma^< \cdot \mathbf{G}^A](t, t') + \mathbf{h}(t) \mathbf{G}^<(t, t') \quad (8)$$

with notations $[f \cdot g](t, t') = \int_{t_0}^{\infty} d\bar{t} f(t, \bar{t}) g(\bar{t}, t')$, $\Sigma^{\lessgtr, A, R} = \sum_{\alpha} \Sigma_{\alpha}^{\lessgtr, A, R}$, and $f^A(t, t') = [f^R(t', t)]^{\dagger}$ ($f \in G, \Sigma$). The self-energy for electrodes by definition is given by

$$\Sigma_{\alpha}^A(t, t') = i\Theta(t' - t) \mathbf{h}_{D\alpha}(t) \exp \left\{ i \int_t^{t'} \mathbf{h}_{\alpha}(\bar{t}) d\bar{t} \right\} \mathbf{h}_{\alpha D}(t') \quad (9)$$

$$\Sigma_{\alpha}^<(t, t') = i\mathbf{h}_{D\alpha}(t) f_{\alpha}(\mathbf{h}_{\alpha, t=t_0}) \exp \left\{ i \int_t^{t'} \mathbf{h}_{\alpha}(\bar{t}) d\bar{t} \right\} \mathbf{h}_{\alpha D}(t') \quad (10)$$

Here, $\Theta(t' - t)$ is the Heaviside step function, \mathbf{h}_{α} is the Kohn-Sham matrix of the isolated electrode α , and f_{α} is the Fermi distribution function for $\alpha \in L, R$.

B. Wide-band limit approximation for the dissipation function Q_{α}

For efficient computations of equation of motion in Eqs. (7) and (8), the wide-band limit (WBL) approximation²⁸ is introduced for L and R electrodes by the following valid conditions: (1) the bandwidths of L and R electrodes are relatively larger than the spectral width of states which are involved in electron transport; (2) the linewidths (the imaginary part of self-energy for electrodes) are assumed to be energy-independent, resulting in the requirement for an electrode's density of state and device-electrode couplings to be slowly varying in energy; and (3) the level shifts of electrodes via bias are approximated to be constant for all energy levels.

Solving the problem within the wide-band limit is not necessary. However WBL considerably speeds up the calculation and is a very good approximation model for simple metal contacts at comparatively low bias. The approximated self-energy now is determined at Fermi level of the systems without bias, and is split up into two real matrices, one hermitian level shift Λ_α and one anti-hermitian linewidth Γ_α . Equations. (9) and (10) can be rewritten as:

$$\Sigma_\alpha^{R,A}(t, t') = (\Lambda_\alpha \mp i\Gamma_\alpha) \delta(t - t') \quad (11)$$

Here, Λ_α and Γ_α are related by the Kramers-Kronig relation²⁹. According to the derivation in appendix B, the dissipation term for electrodes L and R can be given as¹⁵:

$$\mathbf{Q}_\alpha(t) = \mathbf{K}_\alpha(t) + \mathbf{K}_\alpha^\dagger(t) + \{\Gamma_\alpha, \sigma(t)\} + i[\Lambda_\alpha, \sigma(t)] \quad (12)$$

with the definition of $\mathbf{K}_\alpha(t)$ as:

$$\begin{aligned} \mathbf{K}_\alpha(t) = & -\frac{2i}{\pi} \mathbf{U}_\alpha(t) \int_{-\infty}^{\infty} \frac{f_\alpha(\epsilon) e^{i\epsilon t}}{\epsilon - \mathbf{h}_D(0) - \sum_\alpha (\Lambda_\alpha - i\Gamma_\alpha)} d\epsilon \Gamma_\alpha \\ & -\frac{2i}{\pi} \int_{-\infty}^{\infty} [\mathbf{I} - \mathbf{U}_\alpha(t) e^{i\epsilon t}] \frac{f_\alpha(\epsilon)}{\epsilon - \mathbf{h}_D(t) - \sum_\alpha (\Lambda_\alpha - i\Gamma_\alpha) + V_\alpha(t) \mathbf{I}} d\epsilon \Gamma_\alpha \end{aligned} \quad (13)$$

and

$$\mathbf{U}_\alpha(t) = e^{-i \int_0^t [\mathbf{h}_D(\bar{t}) + \sum_\alpha (\Lambda_\alpha - i\Gamma_\alpha) - V_\alpha(\bar{t}) \mathbf{I}] d\bar{t}} \quad (14)$$

Together with the EOM for $\sigma_D(t)$ in Eqs. (3) and (4), one now can calculate the transient electron density of the device and the boundary currents in Eq. (5).

C. Calculations of self-energy matrixes Λ and Γ

We can express the retarded self-energy for the contact with electrode α in the energy domain¹⁵ as:

$$\Sigma_\alpha^r(E) = \mathbf{h}_{D\alpha} \mathbf{G}_\alpha^r(E) \mathbf{h}_{\alpha D} \quad (15)$$

Considering the semi-infinite electrodes, the periodic Au(111) lattices can be divided into principle layers (PLs) along the transport direction (see Fig 1). Here, the PLs are chosen wide enough so that only interactions between the nearest PLs need to be considered; i.e. the coupling matrix $\mathbf{h}_{D\alpha}$ between contact α and device region D will be restricted to one PL. Consequently only the surface block of \mathbf{G}_α^r , the surface green function $\mathbf{G}_\alpha^{r,s}$, is needed for calculating Eq. (15). This work adopts an iterative method³⁰ to calculate the surface green

function that includes properties of the semi-infinite lattices. In principle, the self-energy matrices $\mathbf{\Gamma}$ and $\mathbf{\Lambda}$ for wide-band approximation are calculated at Fermi level as

$$\mathbf{h}_{D\alpha} \mathbf{G}_{\alpha}^{r,s}(E_F) \mathbf{h}_{\alpha D} = \mathbf{\Lambda}_{\alpha} - i\mathbf{\Gamma}_{\alpha} \quad (16)$$

D. Correction of the device Hamiltonian for transient variations of electron densities using the capacitive network model

For the open quantum system, the device Hamiltonian should take the general form

$$\mathbf{h}_D = \mathbf{h}_D^0(q_0) + \delta\mathbf{h}_D(\delta q) \quad (17)$$

Here, the change of electron density can be calculated by the density matrix σ_D in Eq. (3)

$$\delta n(\vec{r}) = \sum_{\mu\nu} \text{Re}[\rho_{\mu\nu} \chi_{\mu}(\vec{r}) \chi_{\nu}^*(\vec{r})] - n_0(r) \quad (18)$$

as a spatial distribution function, or, alternatively, by

$$\delta q_i = \sum_{\mu \in \{i\}} \sum_{\nu} \text{Re}[\rho_{\mu\nu} s_{D,\nu\mu}] - q_{0,i} \quad (19)$$

for atom i . Here, $n_0(r)$ and $q_{0,i}$ are the reference atomic charges chosen for neutrality, \mathbf{s}_D is the device overlap matrix, and $\chi_i(\vec{r})$ is a set of local basis functions used in the tight-binding method. According to a Taylor expansion of the total energy around the reference density, this change of charge density can result in corrections to the Hartree and the exchange-correlation potentials^{31,32} for the device Hamiltonian as in Eq. (17), and it is continuously renewed with the density matrix in Eq. (3). We simplify the correction of the device Hamiltonian $\delta\mathbf{h}_D$ by retaining only the Hartree potential δV_H (assuming the exchange-correlation term is insignificant in the mean-field scope), which obeys the three-dimensional Poisson's equation

$$\nabla^2 \delta V_H(r) = -\delta n(\vec{r}) \quad (20)$$

with the boundary conditions imposed by the lead potentials. The conventional Poisson solution is based on spatially-discretized grids for numerically iterative processes, and can be time-consuming for large systems. So it is convenient to develop an approximately analytical model.

Extending the idea of the muffin-tin (MT) approximation, each atom i can define a spherical region (MT-sphere) that bounds the total excess charges δq_i from Eq. (19). The paired parts of charges inside different neighboring MT-spheres are considered as capacitance effects³³. All these spheres of atoms in the system then further construct a capacitance network architecture that supplies an analytical solution for the Poisson equation³⁴. In principle, the capacitances are treated as a combination of the electrostatic capacitance c_e and quantum capacitance c_Q ³³. Herein, the quantum capacitance is assumed to be less dominant than the electrostatic capacitance for δq_i and is ignored in this present work.

Replacing the spatial solution (∇_r^2) of Poisson's equation by the atomic-site solution (∇_i^2) of the capacitive model^{35,36}, we can rewrite Eq. (20) by a matrix-form equation $\hat{\mathbf{C}}\tilde{\mathbf{V}} = \tilde{\mathbf{Q}}$

$$c_{ij} = 4\pi\epsilon \frac{\bar{a}_{ij}^2}{|r_{ij}|} \left(1 + \frac{\bar{a}_{ij}^2}{|r_{ij}|^2 - 2\bar{a}_{ij}^2} + \dots \right) \quad (21)$$

$$\hat{C}_{ij} = \sum_{k \in \{1NN\}_{i,con}} \delta_{i,j} c_{ik} + \sum_{k \in \{1NN\}_i} \delta_{i,j} c_{ik} - \delta_{j,k} c_{ij} \quad (22)$$

$$\vec{Q}_i = e \cdot \delta q_i + e \cdot \delta q_{d,i} + \sum_{k \in \{1NN\}_{i,con.}} \delta_{j,k} c_{ij} V_{con,j} \quad (23)$$

Here, the matrix elements of $\hat{\mathbf{C}}$ are calculated in a two-center approximation as proposed by the tight-binding model¹⁵, obeying the formal condition $e\delta q_i + e\delta q_{d,i} = \sum_j c_{ij}(\delta V_i - \delta V_j)$. The notation $\{1NN\}_i$ is the group of the first nearest-neighbor (NN) atoms in the device region for atom i , and $\{1NN\}_{i,con.}$ is the group of the first nearest-neighbor atoms in the lead region for device atom i . Extending the system by using $\{nNN\}$ ($n \in 1, 2, \dots$) couplings is also reasonable, because the capacitance value c_{ij} diminishes with the increasing separation $|r_{ij}|$ as in Eq. (21). Herein, c_{ij} defines the capacitance between two ideal metal spheres, and $|r_{ij}|$ is the spatial distance between atoms i and j . \bar{a}_{ij} is the effective muffin-tin radius for atoms i and j and is defined by $\bar{a}_{ij} = (r_{MT,i} + r_{MT,j})/4$ in this work. $\tilde{\mathbf{V}} \equiv (\delta V_1, \delta V_2, \dots, \delta V_N)$ is the potential vector with the components being the electrostatic potential for device atoms $i \in \{1, \dots, N\}$. $V_{con,j}$ is the potential of lead atom j imposed by boundary conditions. δq_i is the charge density obtained by Eq. (19), and $\delta q_{d,i}$ represents the defect charge for atom i . By linear algebra the potential vector $\tilde{\mathbf{V}}$ can be easily solved using $\tilde{\mathbf{V}} = \hat{\mathbf{C}}^{-1}\tilde{\mathbf{Q}}$. For instance, in a 1-dimensional homogeneous system having 4 atoms L-A-A-R, the capacitance between nearby atoms is denoted as c , and the biases are denoted as v_L and v_R for lead atoms L and R, respectively. There are no excess charges ($\delta q = 0$) inside the MT-sphere of device atoms A. In this way, the 2x2 capacitance matrix has components $\hat{C}_{11} = \hat{C}_{22} = 2c$

and $\hat{C}_{12} = \hat{C}_{21} = -c$. The charge vector is $\tilde{\mathbf{Q}}^t = [cv_L \ cv_R]$. One then can obtain the electrostatic potentials for the two atoms A as $\tilde{\mathbf{V}}^t = [2v_L + v_R \ v_L + 2v_R]/3$, agreeing with the free-space Poisson solution.

Figures (2-3) illustrate 2-dimensional examples with a comparison between the numerically iterative solution and the analytical capacitance model. In order to solve the spatial Poisson equation in Eq. (20), the density function $\delta n_i(r)$ for two-dimensional systems is assumed to be:

$$\delta n_i(r) = \frac{\delta q_i}{2\pi\eta^2} e^{-\frac{|r-R_i|}{\eta}} \quad (24)$$

This is according to the symmetry assumption¹⁵, where R_i is the position for atom i , and η is associated with the effective radius of the MT-sphere by $\eta \propto r_{MT,i}$ (use $\eta = r_{MT,i}$ for examples in Figs. (2-3)). The obtained potential $\delta V_H(r)$ is projected on the atomic sites through

$$\delta V_i = \frac{\int d\mathbf{r} \delta V_H(\mathbf{r}) e^{-\frac{|r-R_i|}{\eta}}}{\int d\mathbf{r} e^{-\frac{|r-R_i|}{\eta}}} \quad (25)$$

for a comparison with the analytical solution $\tilde{\mathbf{V}}$ in this work. We note that the analytical model associated with orientatingly capacitive couplings implies a spatial density function beyond the symmetry assumption. As indicated in Figs. (2-3), the analytical solution shows comparable results with that by the numerically-iterative method. It is emphasized that the analytical model turns inefficient at large biases or strong density variations, because the MT sphere cannot accurately account for the distorted and displaced electron density distribution from the nucleus.

The relevant parameters of the MT radius used herein are $r_{MT}(Si) = 1.164\text{\AA}$, $r_{MT}(O) = 0.947\text{\AA}$, $r_{MT}(Au) = 1.376\text{\AA}$, and $r_{MT}(P) = 1.377\text{\AA}$. All computations are operated in a workstation having 2xCPU(E5-2690 v2) and 128G of DRAM. Fortran source codes can be downloaded online³⁷.

III. NUMERICAL RESULTS

A. Atomic Electrodes: Au(111) Nanotubes

This research uses Au(111) nanotubes as atomic electrodes. The length ℓ of the Au-Au bond is determined with geometry relaxations of Au bulk in the SIESTA program^{22,23},

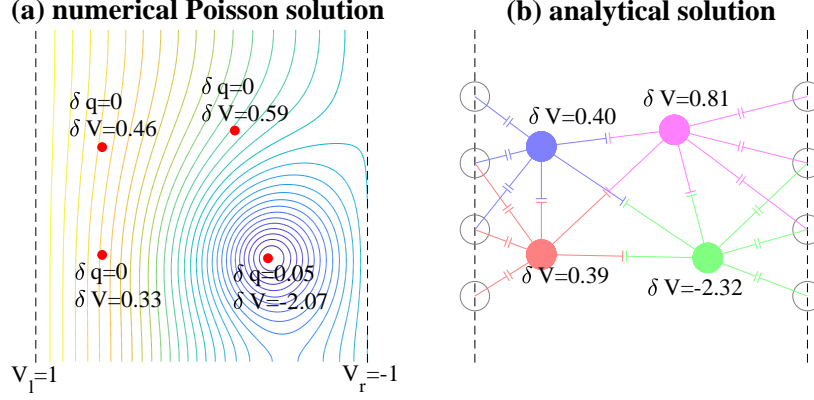


FIG. 2. Profile of Hartree potential δV_i of the first $9 \times 9\text{-}\text{\AA}^2$ structure, solved by (a) the numerical Poisson solution and (b) the analytical solution. Four atoms with specified charges δq (see Figure (a)) are placed between two leads and have $r_{MT} = 1\text{\AA}$. In (a) the additional spatial function $\delta V(r)$ is illustrated by the contour curves. In (b) each boundary condition of the electrostatic potential is represented by four lead atoms.

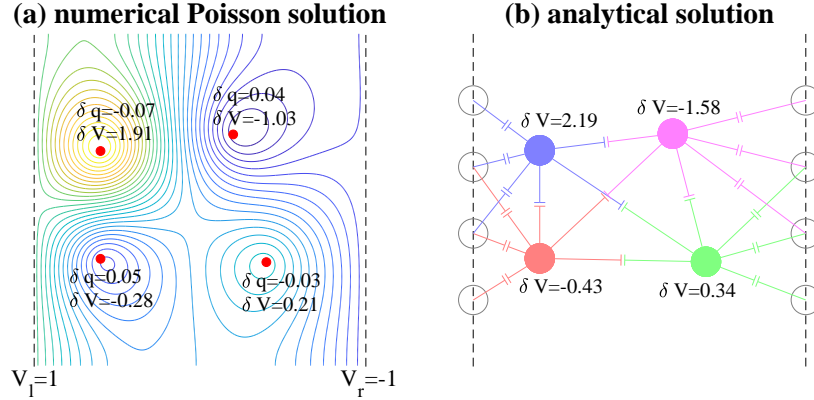


FIG. 3. Profile of Hartree potential δV_i of the second $9 \times 9\text{-}\text{\AA}^2$ structure, solved by (a) the numerical Poisson solution and (b) the analytical solution. Relevant setups are the same with that in Fig. 2, except for atom charge δq .

and the obtained value is $\ell=2.8785\text{ \AA}$ (lattice constant $a=\sqrt{2}\ell=4.0708\text{ \AA}$, similar to experimental value³⁸ 4.0782 \AA). The effects of core electrons are evaluated with norm-conserving pseudopotentials in local density approximation (Ceperley-Alder exchange-correlation potential^{39,40}), which are generated by the ATOM program^{22,41}. The valence electrons of Au is calculated in the s-d hybridized configuration⁴². All the calculations for

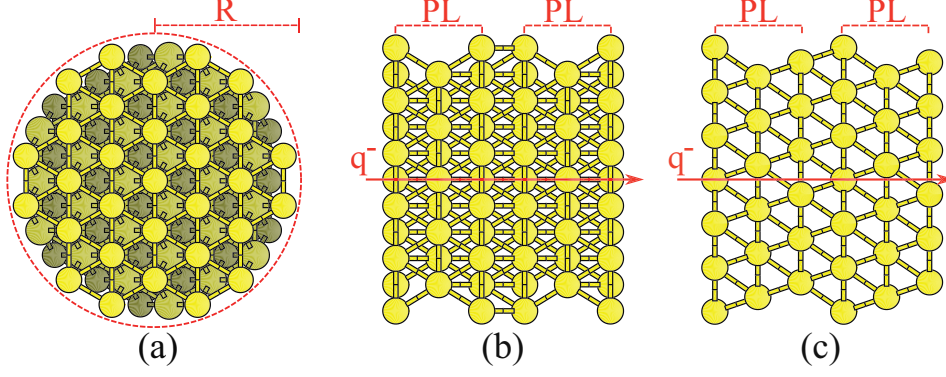


FIG. 4. Ball-stick representation of the Au(111) nanotube in (a) the longitudinal perspective and in (b-c) two lateral perspectives. The radius of the cross section in (a) is set as $R=2a$. Two of the principle layers (PL) arranged along the longitudinal (transport) direction in (b-c) represent a segment of the nanotube. q^- indicates the quasi one dimensional (red arrow) charge transport.

nanotubes are performed on $8 \times 8 \times 8$ Monkhorst-Pack grids in reciprocal spaces, with an electronic temperature of 300K. Figure 4 shows (a) the longitudinal perspective and (b-c) two lateral perspectives for a finite segment of Au(111) nanotubes. In actual computations, the nanotube is set as an infinite stack of principle layers (PL) along the axial (longitudinal) direction, and has cross-section radius R . Figure 5 shows the normalized density of states (DOS) for Au bulk and Au(111) nanotubes, where the radii of the nanotubes are set as $R=0.5a$, $R=2.0a$, and $R=4.0a$, respectively. E_F is the Fermi level corresponding to the mentioned system. In Fig. 5, DOS of Au bulk shows metallic properties as reported in the literature⁴³. When increasing the cross-section radius R , the DOS functions of Au(111) nanotubes at energies near E_F change from discrete to uniform distributions, depicting the transfer of systems from 1D-nanotube to 3D-bulk structures. In this work, we use Au(111) nanotubes with $R=2a$ for semi-infinite electrodes in transport problems. This adoption (setting $R=2a$) meets the requirement of slowly-varying DOS for the wide-band limit (WBL) condition²⁸, and demands computation resources that are affordable.

B. Doped Si-SiO₂ quantum dots

This research investigates the silicon quantum dots with diameters around 1.0 nm that are embedded in β -cristobalite SiO₂ matrix. The dopant phosphorus (P) atoms are placed

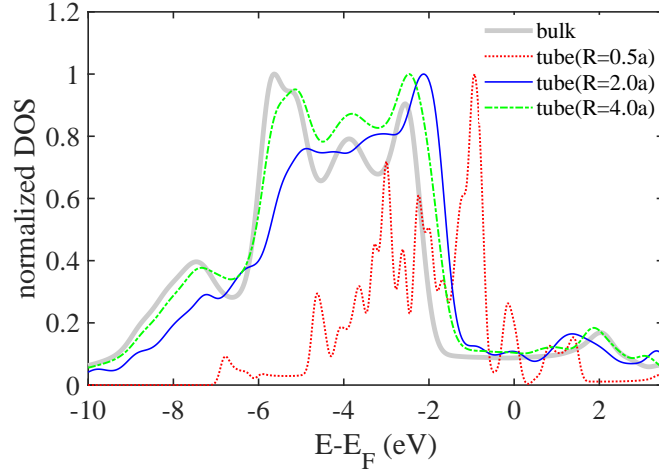


FIG. 5. Normalized density of states (DOS) for Au bulk and infinite Au(111) nanotubes, in which the radii of the nanotubes are set as $R=0.5a$, $R=2.0a$, and $R=4.0a$.

inside quantum dots due to their energetically-favored formation of structures²¹ (see Fig. 6). Lattice constants are determined with geometry relaxations in the SIESTA program. The obtained values are 5.5001 \AA (5.4306 \AA by experiment³⁸) for the Si diamond structure and 7.46831 \AA ($7.160\text{-}7.403 \text{ \AA}$ in textbooks^{38,44}) for β -cristobalite silica. The energy band diagram of Si-SiO₂-slabs heterojunctions by using Anderson's rule is investigated through Fig. 7, in which the vacuum levels (green dotted lines) of Si and SiO₂ slabs are aligned at the same energy. Here, the vacuum level is defined as the effective potential ϕ (adding local pseudopotential, Hartree potential, and exchange-correlation potential) at zero-density points near the surface of slabs having 35 atomic layers. All calculations are performed at Γ -point of the reciprocal space. As indicated in Fig. 7, the vacuum levels are 1.064 eV and 1.626 eV for Si-slab and SiO₂-slab, respectively, corresponding to working functions $W_{Si}=4.46 \text{ eV}$ and $W_{SiO_2}=4.52 \text{ eV}$. The experimental value³⁸ is $4.60 \leq W_{Si} \leq 4.91 \text{ eV}$. The computed energy gaps are 1.17 eV for bulk silicon and 7.7 eV for β -cristobalite silica, which can be compared with the experimental values of 1.1 eV and 9.0 eV , respectively. The valence band offset (VBO) and conduction band offset (CBO) for Si-SiO₂ heterojunctions are estimated to be 3.18 eV and 3.31 eV , respectively. The obtained VBO values are smaller than experimental measurements^{45,46} with $VBO=4.6 \text{ eV}$ and $CBO=3.1 \text{ eV}$. Several theoretical works using hopping mechanisms^{21,47,48} give $VBO \approx 2.6 \text{ eV}$ and $CBO \approx 3.9 \text{ eV}$.

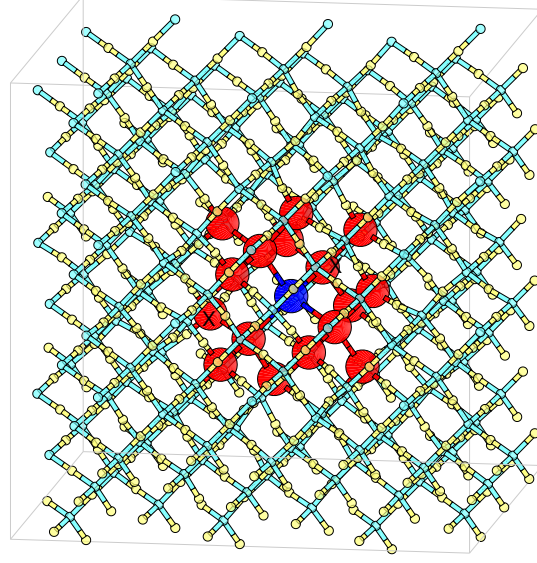


FIG. 6. Schematics of Si Quantum Dot (red atoms) embedded in SiO_2 matrix (light cyan-yellow atoms). The phosphorus atom P (blue atom) is doped inside the quantum dot for the 1P-doping condition. Two red atoms with X marks denote the doping locations inside the quantum dot and at the interface, respectively, for the 2P-doping condition.

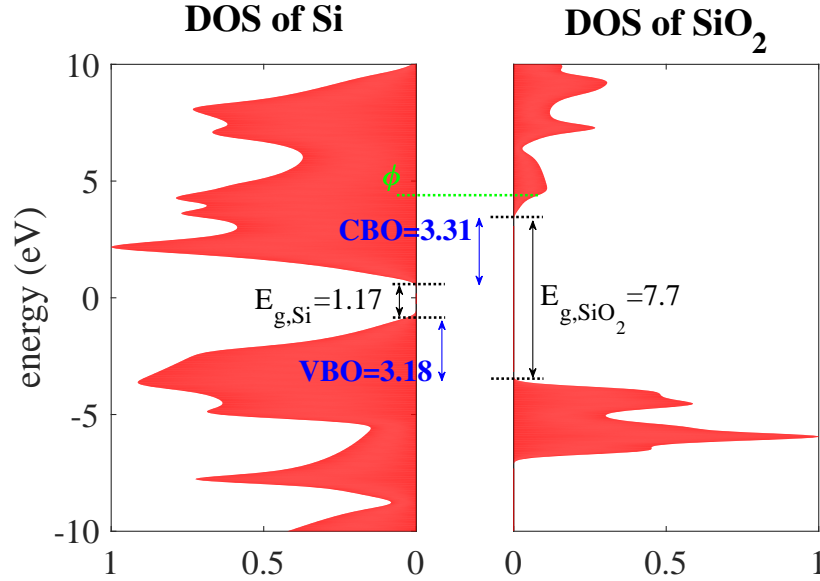


FIG. 7. Band diagrams of Si- SiO_2 -slabs heterojunction by Anderson's rule. The density of state at equilibrium is arranged according to a hypothetical flat vacuum level. The computed energy gaps are $E_{g,\text{Si}}=1.17$ eV and $E_{g,\text{SiO}_2}=7.7$ eV. The valence band offset VBO is 3.18 eV and the conduction band offset CBO is 3.31 eV.

With relevant material parameters, the Si-SiO₂ quantum-dot device in Fig. 6 is constructed from a $3 \times 3 \times 3$ supercell of β -cristobalite silica by removing O atoms in a cut-off box. Figure 8 reports the eigenvalue spectra for the undoped, 1P-doping, and 2P-doping structures after relaxation processes, using the corresponding initial geometries in Fig. 6. The spectrum energies are aligned using the SiO₂ states (deep valence states), and are shifted with the reference of the fermi level of the undoped structure. Black and gray circles mark the highest occupied molecular orbital (HOMO) and lowest unoccupied molecular orbital (LUMO) states, respectively. The green dotted line represents the fermi level of the corresponding structure. For the undoped structure, SiO₂ atoms get amorphized after relaxations owing to the strained interface between Si and SiO₂ lattices. Its electronic spectrum in Fig. 8(a) exhibits distinct properties from that in Fig. 7. As evidenced by previous investigations⁴⁹, the occurrence of strain-induced electron levels plays a fundamental role in opto-electronic dynamics. For the 1P-doping system, the odd number of electrons lead to the spin-dependent energy spectrum in Fig. 8(b), which depicts a clear donor behavior and agrees well with previous works^{21,50}. In this study, the 2P-doping structure in Fig. 8(c) is adopted for the following advantages: (i) high conductivity at a low bias V due to the raising fermi level and decreasing energy gap, compared to the undoped structure; and (ii) spin independence for excluding unknown spin parameters and better computational efficiency.

C. Steady transport properties of open quantum-dot systems

The open transport system of quantum dots is constructed in Fig. 9. The device region, i.e. Si-based quantum dot (red atoms) and SiO₂ matrix (small light cyan-yellow atoms), is enclosed by two semi-infinitely long Au wires. Two dopant atoms (phosphorus; blue atoms) are stochastically placed inside the quantum dot and at the Si-SiO₂ interface, respectively. It is assumed that the positions of atoms of Au electrodes are under constraint by the experimental set-ups, while the atoms of the doped Si-SiO₂ quantum dot are in equilibrium according to geometry relaxations by the SIESTA program. The distance between the nearest cross sections of silica and gold boundaries are initially set to be 1.8 Å in this work.

By applying non-equilibrium green functions for steady transport problems³³, the transmission function of the quantum-dot system is obtained as shown in Fig. 10. In Fig. 10(a),

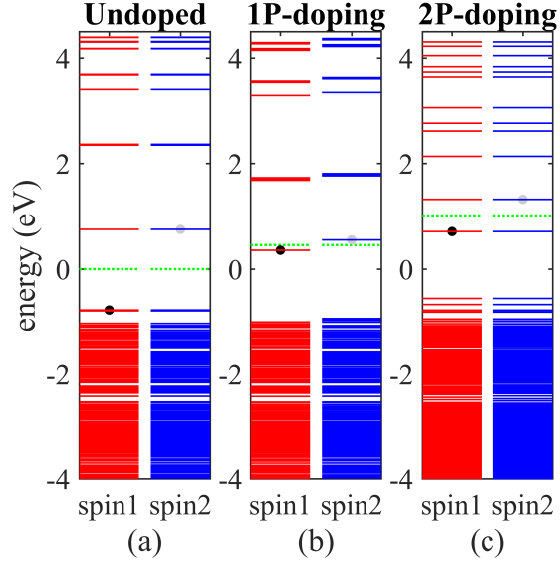


FIG. 8. Spin-up and spin-down spectra of (a) undoped, (b) 1P-doping, and (c) 2P-doping systems. Energies are aligned using the embedding SiO_2 states, and are shifted with the reference of the Fermi level of the undoped structure. Black and gray circles mark HOMO and LUMO states, respectively. The green dotted line represents the Fermi level of the corresponding system.

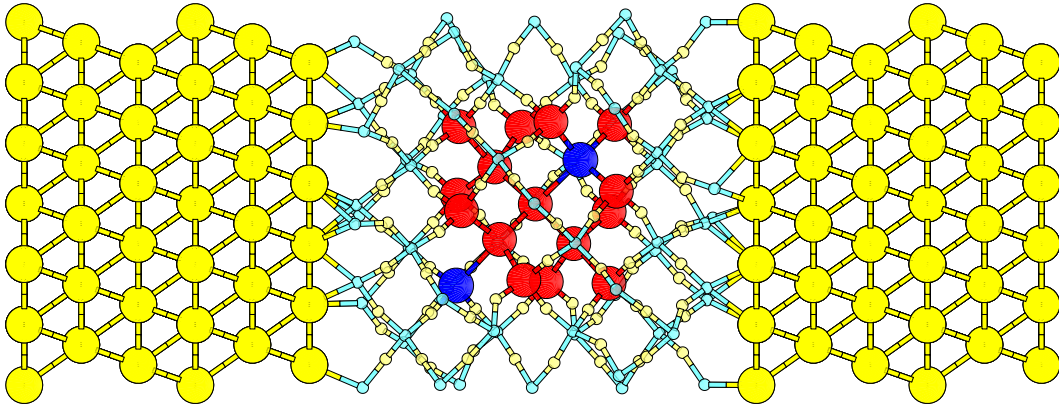


FIG. 9. Schematics of a Si-based (red atoms) quantum dot embedded in β -cristobalite SiO_2 matrix (small light cyan-yellow atoms), where two dopant atoms (blue phosphorus atoms) are placed inside the quantum dot and at the Si- SiO_2 interface, respectively. The device is enclosed between two semi-infinitely-long Au(111) wires (larger yellow atoms) with an applied voltage.

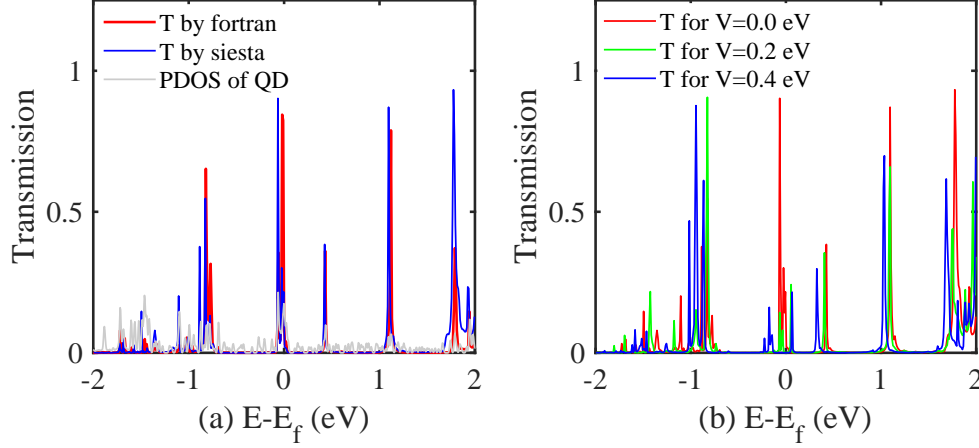


FIG. 10. (a) Transmission functions of the quantum-dot system ($V=0.0$ eV) using SIESTA and Fortran programs, in order to compare with the projected density of state (PDOS) of Si-SiO₂ QDs. (b) Transmission functions of the quantum-dot system calculated by SIESTA programs at different voltage biases.

the transmission function T (blue curve) is calculated by SIESTA::Transiesta programs, and is associated with the projected density of state (PDOS; gray curve) of the Si-SiO₂ quantum dot. The red-curve transmission function is calculated by Fortran code, with given hamiltonian and overlap matrices that serve as the initial values for time-dependent non-equilibrium green functions in transient transport problems below. Numerical results demonstrate that the conductance channels in the transmission function T are comparable to the density of states of the Si-SiO₂ quantum dots as expected. Figure 10(b) depicts transmission functions calculated by SIESTA programs at different voltage biases. It is found that the energy gap of the quantum-dot device varies with bias and one can infer the requirement of corrections of the Hamiltonian for variations of charge densities in transient problems. We also note that the quantum-dot system presents finite conductance at near zero bias, similar to the analysis in Nuria's work²¹. This conductance associated with the transmission function at the fermi level decreases with an increasing bias as shown in Fig. 10(b).

D. Time-dependent electron transport in open quantum-dot systems

This section studies the time-dependent electron transport for the quantum-dot system in Fig. 9. Additional parameters and numerical methods are as follows: time step $\delta t = 5as$,

voltage function $V_f(t) = V_{dc} [1 - \exp^{-t/\tau}] + V_{ac} \cos(\omega t)$ with $\tau = 2fs$, globally-adaptive integrator treating singularities in the energy domain, and the fourth-order RungeKutta methods (RK4) for solving the time-differential equation. Here, we adopt the linear extrapolation of the density matrix σ_D (Eq. 3) during the iterative process by RK4. Figure 11(a) shows transient currents by our TDNEGF codes with and without corrections for charge transfer effects (CET). The voltage functions are symmetrically set by $V_L = V_{f,V_{dc}=0.5V,V_{ac}=0V}$ and $V_R = V_{f,V_{dc}=-0.5V,V_{ac}=0V}$ for the left and right electrodes, respectively. Numerical results show that in the long-time limit the currents asymptotically approach the value of the steady solutions by SIESTA (see the insect diagram). Besides, the inclusion of charge transfer effects presents insignificant corrections for the steady currents at a low bias condition, but results in obviously different transient transport processes. Figure 11(b) shows the transient electron number of the device and the integrals of boundary currents, obeying the continuity equation for the device region. Besides, the curves depicts that the calculation including CET requires longer time to bring the system into equilibrium, inferring a slow redistribution process of the charge density. Figure 11 indicates, as expected, that the charge transfer effects are insignificant for the quantum-dot device under a low DC bias.

In Fig. 12(a), we study the transient currents for the quantum-dot devices under AC bias voltages. The voltage functions are asymmetrically set by $V_L = V_{f,V_{dc}=0.1V,V_{ac}=0V}$ and $V_R = V_{f,V_{dc}=-0.1V,V_{ac}=0.4V}$ for the left and right electrodes, respectively. Here the AC frequency is $\omega = 0.835 \times 10^{15}$. For the quantum-dot device including charge transfer effects, the interfacial current I_L of the left electrode exhibits continuous oscillations; while I_L quickly reduces to a constant value for the calculation without charge transfer effects. The interfacial current I_R of the right electrode, however, is always oscillatory due to the driving of the AC potentials at the right electrode. This observation demonstrates the oscillation of charge densities inside the quantum-dot device via CTE algorithms. To correlate with practical measurements, we calculate the average current $I_{avg.}(t)$ by averaging $I(t)$ over one period $T = 2\pi/\omega$. Numerical results of $I_{avg.}(t)$ are shown in Fig. 12(b). In its inset diagram, the effective currents, no matter with and without including charge transfer effects, asymptotically converge into similar values. We attribute the similarity of the asymptotical currents to the low average bias and no trigger of photon-assisted events. Fig. 12(c), the same with Fig. 11(b), validates the algorithms by the continuity equation.

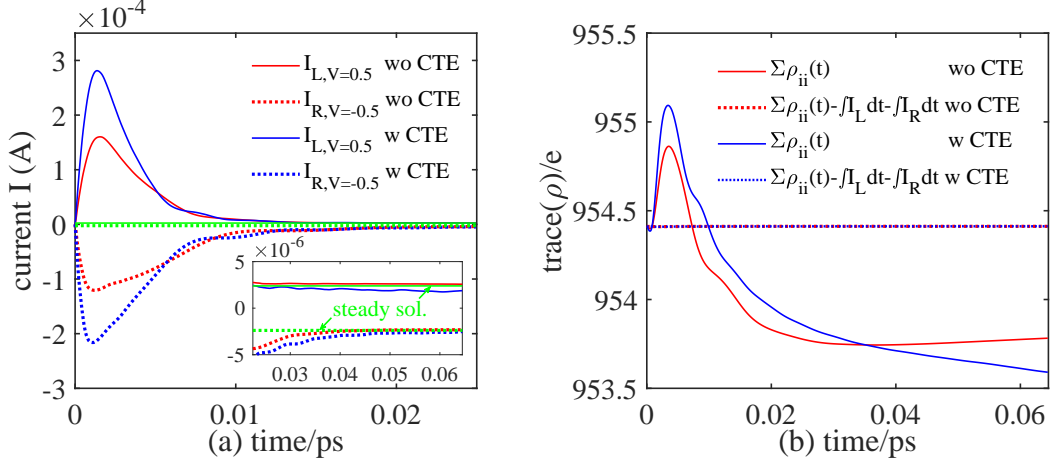


FIG. 11. (a) Transient current I of quantum-dot devices at a symmetry DC bias $V_{dc}=0.5$ V with/without including charge transfer effect (CTE). The inset diagram shows that the currents asymptotically approach the value of the steady solution by SIESTA (green curves). (b) Transient charge numbers of the quantum-dot device with/without including CTE. After applying bias, part of electrons ($\Sigma\rho_{ii}$, solid curves) participate in the inter-orbital transferring process ($\int I_L dt + \int I_R dt$). The dot curves show the conservation of total charges.

IV. CONCLUSIONS

To explore the photoelectric responses of hybridized semiconductor-biology systems for applications, this research preliminarily proposes an approximate analytical model to efficiently calculate the transient properties of bio-compatible quantum-dot systems under time-dependent external potentials. The numerical results in the low DC bias and long-time limits reduce to conventional steady solutions where the charge transfer effects are insignificant. For the cases using asymmetry AC biases, however, numerical calculations show distinct difference between the transient currents of the quantum-dot devices with and without corrections of charge transfer effects; while the effective (average) currents asymptotically converge into similar values. The results reveal the underlying oscillations of charge densities inside the device. With extending electron dynamics for interactions of light or environments by the present TDNEGF technique in the future, this work targets to investigate multi-scale QM-MM (Quantum Mechanism-Molecular Mechanism) dynamics for the biomedicine study.

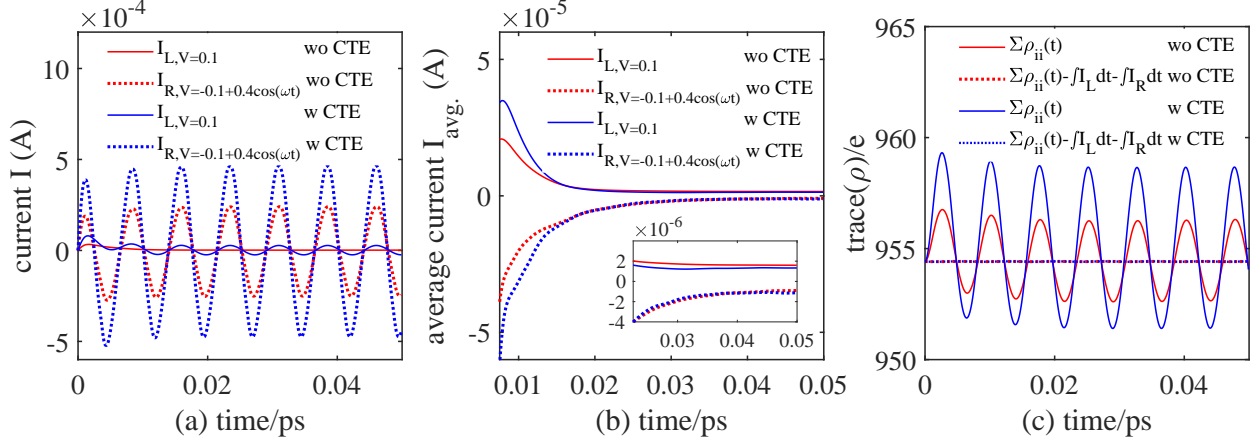


FIG. 12. (a) Transient current I of quantum-dot devices at AC bias $V_L=0.1\text{V}$ and $V_R=-0.1+0.4\cos(\omega t)$ V, with/without including charge transfer effect (CTE). Here the AC frequency is $\omega = 0.835 \times 10^{15}$. With including CTE, I_L exhibits continuous oscillations of interfacial currents. (b) Effective currents $I_{avg.}$ by averaging $I(t)$ in (a) over one period $T = 2\pi/\omega$. The inset diagram shows that the effective currents, with/without including CTE, asymptotically converge into similar values. (c) Transient charge numbers of the quantum-dot device with and without including CTE. The dot curves show the conservation of total charges.

V. ACKNOWLEDGEMENT

This work was supported by ChiMei Visual Technology Corporation.

Appendix A: Equation of motion for Green functions

The Hamiltonian operator $\hat{\mathbf{h}}$ for open transport systems without spin notations can be given by

$$\hat{\mathbf{h}} = \sum_{k_\alpha} h_{\alpha,k_\alpha} n_{k_\alpha} + \sum_{m,n} h_{D,mn} a_m^\dagger a_n + \sum_{m,k_\alpha} h_{D\alpha,mk_\alpha} a_m^\dagger a_{k_\alpha} + h_{\alpha D,k_\alpha m} a_{k_\alpha}^\dagger a_m \quad (\text{A1})$$

The first term describes the α_{th} electrode with state k_α , the second term is for the device in geometry region D, and the third term is for the coupling between the device and the electrode α .

In this appendix, the algorithm of the time-dependent non-equilibrium green function is addressed for systems under the following conditions: during $t < t_0$, the system is in

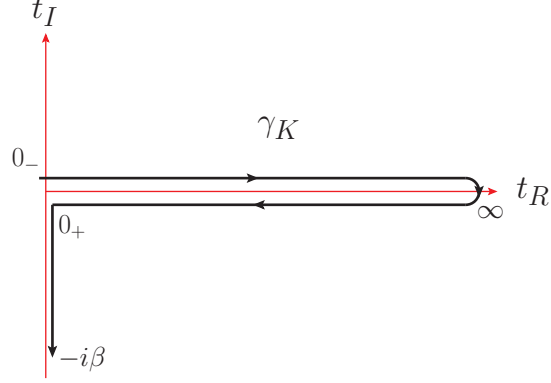


FIG. 13. The Keldysh contour γ_K is an oriented contour having endpoints at 0_- and $-i\beta$. β is the inverse temperature. The contour is composed of a forward branch going from $t = 0_-$ to $t = \infty$, a backward branch coming back from $t = \infty$ to $t = 0_+$, and a vertical (thermic) track on the imaginary times axis between 0_+ and $-i\beta$. z and z' define variables along γ_K .

thermal equilibrium at an inverse temperature β and chemical potential μ . At times $t \geq t_0$, the system departs from the equilibrium conditions after applying external voltages. Here, the response of the spin to external fields is ignored, resulting in diagonal green-function and self-energy matrices with respect to the spin parameter. The initial condition is defined by the ground state of the system.

For time-dependent electron transport problems, one begins with the one-particle green function on the Keldysh contour γ_K (see Fig. 13). This green function is defined as the ensemble average of the contour-ordered product of electron creation and annihilation operators in the Heisenberg picture,

$$G_{rs}(z, z') = -i \langle T_C [a_r(z) a_s^\dagger(z')] \rangle \quad (\text{A2})$$

Here, r, s present states of L(left-electrode), R(right-electrode), and D(device). z and z' define complex variables along the contour γ_K . T_C is the time-ordering operator. The creation operator a^\dagger and annihilation operator a obey the equation of motion

$$i \frac{d}{dz} a(z) = [a(z), h(z)] = h(z) a(z) \quad (\text{A3})$$

$$i \frac{d}{dz} a^\dagger(z) = [a^\dagger(z), h(z)] = -h(z) a^\dagger(z) \quad (\text{A4})$$

Here, the anticommutator relation for fermions have been used, i.e. $\{a_r, a_s\} = \{a_r^\dagger, a_s^\dagger\} = 0$ and $\{a_r, a_s^\dagger\} = \langle r|s \rangle$ with orthonormal state bases r and s . Combining Eqs. (A3-A4) and

(A2), the equation of motion for the green function can be given as:

$$\left[i \frac{d}{dz} - h(z) \right] G(z, z') = \delta(z, z') \mathbf{1} \quad (\text{A5})$$

$$G(z, z') \left[-i \frac{d}{dz'} - h(z') \right] = \delta(z, z') \mathbf{1} \quad (\text{A6})$$

Here, the green function follows Kubo-Martin-Schwinger (KMS) boundary conditions on the imaginary axis in γ_K . $h(z)$ is the single-particle Hamiltonian.

Applying the definition in Eq. (2), the matrix structure of \mathbf{G} has block matrix form:

$$\mathbf{G} = \begin{bmatrix} \mathbf{G}_L & \mathbf{G}_{LD} & \mathbf{G}_{LR} \\ \mathbf{G}_{DL} & \mathbf{G}_D & \mathbf{G}_{DR} \\ \mathbf{G}_{RL} & \mathbf{G}_{RD} & \mathbf{G}_R \end{bmatrix} \quad (\text{A7})$$

Equation (A5) in matrix form is hence given by

$$i \frac{d}{dz} \mathbf{G}(z, z') - \mathbf{h}(z) \mathbf{G}(z, z') = \delta(z, z') \mathbf{1} \quad (\text{A8})$$

Here, the equations for components $\mathbf{G}_{\alpha D}$ and \mathbf{G}_D are

$$\left[i \frac{d}{dz} - \mathbf{h}_D(z) \right] \mathbf{G}_D(z, z') = \delta(z, z') \mathbf{1} + \sum_{\alpha \in L, R} \mathbf{h}_{D\alpha}(z) \mathbf{G}_{\alpha D}(z, z') \quad (\text{A9})$$

$$\left[i \frac{d}{dz} - \mathbf{h}_\alpha(z) \right] \mathbf{G}_{\alpha D}(z, z') = \mathbf{h}_{\alpha D}(z) \mathbf{G}_D(z, z') \quad (\text{A10})$$

By multiplying Eq. (A10) with the green function \mathbf{G}_α , i.e. $\left[-i \frac{d}{dz'} - \mathbf{h}_\alpha(z') \right] \mathbf{G}_\alpha(z, z') = \delta(z, z') \mathbf{1}$ in Eq. (A5), we can obtain $\mathbf{G}_{\alpha D}(z, z')$ as

$$\begin{aligned} \int_{\gamma_K} d\bar{z} \mathbf{G}_\alpha(z, \bar{z}) \left[i \frac{d}{d\bar{z}} - \mathbf{h}_\alpha(\bar{z}) \right] \mathbf{G}_{\alpha D}(\bar{z}, z') &= \int_{\gamma_K} d\bar{z} \left[\left(-i \frac{d}{d\bar{z}} - \mathbf{h}_\alpha(\bar{z}) \right) \mathbf{G}_\alpha(z, \bar{z}) \right] \mathbf{G}_{\alpha D}(\bar{z}, z') \\ &= \int_{\gamma_K} d\bar{z} \delta(z, \bar{z}) \mathbf{G}_{\alpha D}(\bar{z}, z') \\ &= \int_{\gamma_K} d\bar{z} \mathbf{G}_\alpha(z, \bar{z}) \mathbf{h}_{\alpha D}(\bar{z}) \mathbf{G}_D(\bar{z}, z') \\ \mathbf{G}_{\alpha D}(z, z') &= \int_{\gamma_K} d\bar{z} \mathbf{G}_\alpha(z, \bar{z}) \mathbf{h}_{\alpha D}(\bar{z}) \mathbf{G}_D(\bar{z}, z') \end{aligned} \quad (\text{A11})$$

We apply integration by parts and assume the disappearance of electrons at infinite distance. Inserting equation (A11) into equation (A9), the equation of motion for $\mathbf{G}_D(z, z')$ can be obtained as

$$\begin{aligned} \left[i \frac{d}{dz} - \mathbf{h}_D(z) \right] \mathbf{G}_D(z, z') &= \delta(z, z') \mathbf{1} \\ &+ \int_{\gamma_K} d\bar{z} \left[\sum_{\alpha} \mathbf{h}_{D\alpha}(z) \mathbf{G}_\alpha(z, \bar{z}) \mathbf{h}_{\alpha D}(\bar{z}) \right] \mathbf{G}_D(\bar{z}, z') \end{aligned}$$

The term $\sum_{\alpha} \mathbf{h}_{D\alpha}(z) \mathbf{G}_{\alpha}(z, \bar{z}) \mathbf{h}_{\alpha D}(\bar{z}) = \sum_{\alpha} \Sigma_{\alpha}$ is defined as the coupling self-energy $\Sigma(z, \bar{z})$ and the equation is reformulated as

$$\left[i \frac{d}{dz} - \mathbf{h}_D(z) \right] \mathbf{G}_D(z, z') = \delta(z, z') \mathbf{1} + \int_{\gamma_K} d\bar{z} \Sigma(z, \bar{z}) \mathbf{G}_{MM}(\bar{z}, z') \quad (\text{A12})$$

1. Kadanoff-Baym equations

The equations for the device's green function $\mathbf{G}_D(z, z')$ are summarized as:

$$\left[i \frac{d}{dz} - \mathbf{h}(z) \right] \mathbf{G}(z, z') = \delta(z, z') \mathbf{1} + \int_{\gamma_K} d\bar{z} \Sigma(z, \bar{z}) \mathbf{G}(\bar{z}, z') \quad (\text{A13})$$

$$\mathbf{G}(z, z') \left[-i \frac{d}{dz'} - \mathbf{h}(z') \right] = \delta(z, z') \mathbf{1} + \int_{\gamma_K} d\bar{z} \mathbf{G}(z, \bar{z}) \Sigma(\bar{z}, z') \quad (\text{A14})$$

Here, the subscript D is dropped in this subsection for simplicity. Because the lesser green function $\mathbf{G}^<$ is directly related to observable physical quantities, i.e. electron densities and currents, its integro-differential equation is described first. Using the definition of $\mathbf{G}^<(t_-, t_+) = \mathbf{G}(z = t_-, z' = t_+)$ with $t_- < t_+$ and separating the Keldysh contour by real and imaginary segments in Eq. (A13), one gets:

$$\begin{aligned} & \left[i \frac{d}{dt_-} \right] \mathbf{G}^<(t_-, t_+) - \mathbf{h}(t_-) \mathbf{G}^<(t_-, t_+) \\ &= \int_{\text{Re}\gamma_K} d\bar{t} [\Sigma(t_-, \bar{t}) \mathbf{G}(\bar{t}, t_+)] - i \int_{\text{Im}\gamma_K} d\tau [\Sigma(t_-, t_0 - i\tau) \mathbf{G}(t_0 - i\tau, t_+)] \end{aligned} \quad (\text{A15})$$

Adopting common notations f for green functions \mathbf{G} and self-energy Σ in the Keldysh space, we arrive at:

$$f(t, t')|_{f \in \mathbf{G}, \Sigma} = f^{\delta}(t) \delta(t - t') + \Theta(t - t') f^>(t, t') + \Theta(t' - t) f^<(t, t') \quad (\text{A16})$$

$$f^R(t, t')|_{f \in \mathbf{G}, \Sigma} = f^{R, \delta}(t) \delta(t - t') + \Theta(t - t') [f^>(t, t') - f^<(t, t')] \quad (\text{A17})$$

$$f^A(t, t')|_{f \in \mathbf{G}, \Sigma} = f^{A, \delta}(t) \delta(t - t') - \Theta(t' - t) [f^>(t, t') - f^<(t, t')] \quad (\text{A18})$$

$$f^{\lceil}(t, \tau)|_{f \in \mathbf{G}, \Sigma} = f^<(t, t_0 - i\tau) \quad (\text{A19})$$

$$f^{\rceil}(\tau, t)|_{f \in \mathbf{G}, \Sigma} = f^>(t_0 - i\tau, t) \quad (\text{A20})$$

Equation (A15) can be rewritten as

$$\begin{aligned} & i \frac{d}{dt_-} \mathbf{G}^<(t_-, t_+) - \mathbf{h}(t_-) \mathbf{G}^<(t_-, t_+) \\ &= \int_{t_0}^{\infty} d\bar{t} \Sigma^R(t_-, \bar{t}) \mathbf{G}^<(\bar{t}, t_+) + \int_{t_0}^{\infty} d\bar{t} \Sigma^<(t_-, \bar{t}) \mathbf{G}^A(\bar{t}, t_+) - i \int_0^{\beta} d\tau \Sigma^{\lceil}(t_-, \tau) \mathbf{G}^{\rceil}(\tau, t_+) \end{aligned}$$

Alternatively, we have

$$i \frac{d}{dt_-} \mathbf{G}^<(t_-, t_+) - \mathbf{h}(t_-) \mathbf{G}^<(t_-, t_+) = [\Sigma^R \cdot \mathbf{G}^< + \Sigma^< \cdot \mathbf{G}^A + \Sigma^\dagger \star \mathbf{G}^\dagger](t_+, t_-) \quad (\text{A21})$$

with notations $[f \cdot g](t, t') = \int_{t_0}^{\infty} d\bar{t} f(t, \bar{t}) g(\bar{t}, t')$ and $[f \star g](t, t') = -i \int_0^{\beta} d\bar{t} f(t, \tau) g(\tau, t')$.

Equations for the greater green function $\mathbf{G}^>$ can be obtained by similar processes:

$$i \frac{d}{dt_-} \mathbf{G}^<(t_-, t_+) - \mathbf{h}(t_-) \mathbf{G}^<(t_-, t_+) = [\Sigma^R \cdot \mathbf{G}^< + \Sigma^< \cdot \mathbf{G}^A + \Sigma^\dagger \star \mathbf{G}^\dagger](t_-, t_+) \quad (\text{A22})$$

$$i \frac{d}{dt_+} \mathbf{G}^>(t_+, t_-) - \mathbf{h}(t_+) \mathbf{G}^>(t_+, t_-) = [\Sigma^R \cdot \mathbf{G}^> + \Sigma^> \cdot \mathbf{G}^A + \Sigma^\dagger \star \mathbf{G}^\dagger](t_+, t_-) \quad (\text{A23})$$

and,

$$-i \frac{d}{dt_+} \mathbf{G}^<(t_-, t_+) - \mathbf{h}(t_+) \mathbf{G}^<(t_-, t_+) = [\mathbf{G}^R \cdot \Sigma^< + \mathbf{G}^< \cdot \Sigma^A + \mathbf{G}^\dagger \star \Sigma^\dagger](t_-, t_+) \quad (\text{A24})$$

$$-i \frac{d}{dt_-} \mathbf{G}^>(t_+, t_-) - \mathbf{h}(t_-) \mathbf{G}^>(t_+, t_-) = [\mathbf{G}^R \cdot \Sigma^> + \mathbf{G}^> \cdot \Sigma^A + \mathbf{G}^\dagger \star \Sigma^\dagger](t_+, t_-) \quad (\text{A25})$$

Equations (A22)-(A25) are the Kadanoff-Baym equations with symmetry relations of functions $f \in \mathbf{G}, \Sigma$:

$$f^{\geq}(t, t')|_{f \in \mathbf{G}, \Sigma} = -[f^{\geq}(t', t)]^\dagger \quad (\text{A26})$$

$$f^{\dagger\dagger}(t, t')|_{f \in \mathbf{G}, \Sigma} = -[f^{\dagger\dagger}(t', t)]^\dagger \quad (\text{A27})$$

$$G^>(t, t) = -i + G^<(t, t), \text{ at equal time} \quad (\text{A28})$$

$$G^A(t, t') = [G^R(t', t)]^\dagger \quad (\text{A29})$$

2. Approximate equations for fast numerical implementation by neglecting the complex-axis integral

For the equation of motion for the retarded green function $\mathbf{G}^R(t, t')$, one can differentiate Eq. (A17) with respect to t , ignoring the $\mathbf{G}^\delta \delta(t - t')$ term and the complex path in the Keldysh contour,

$$\begin{aligned} i \frac{d}{dt} \mathbf{G}^R(t, t') &= i \delta(t - t') [\mathbf{G}^>(t, t') - \mathbf{G}^<(t, t')] \\ &\quad + \Theta(t - t') \left[i \frac{d}{dt} \mathbf{G}^>(t, t') - i \frac{d}{dt} \mathbf{G}^<(t, t') \right] \end{aligned} \quad (\text{A30})$$

Together with Eqs. (A22) and (A23), Eq. (A30) can be rewritten as

$$\begin{aligned} i \frac{d}{dt} \mathbf{G}^R(t, t') &= \delta(t - t') + \mathbf{h}(t) \Theta(t - t') [\mathbf{G}^>(t, t') - \mathbf{G}^<(t, t')] \\ &\quad + \Theta(t - t') [\Sigma^R \cdot \mathbf{G}^> + \Sigma^> \cdot \mathbf{G}^A - \Sigma^R \cdot \mathbf{G}^< - \Sigma^< \cdot \mathbf{G}^A](t, t') \\ &= \delta(t - t') + \mathbf{h}(t) \mathbf{G}^R + \Sigma^R \cdot \mathbf{G}^R \end{aligned} \quad (\text{A31})$$

For the equation of motion for the lesser green function $\mathbf{G}^<(t, t')$, Eq. (A22), by ignoring complex integration, gives

$$i\frac{d}{dt}\mathbf{G}^<(t, t') - \mathbf{h}(t) \mathbf{G}^<(t, t') = [\boldsymbol{\Sigma}^R \cdot \mathbf{G}^< + \boldsymbol{\Sigma}^< \cdot \mathbf{G}^A](t, t') \quad (\text{A32})$$

For the evaluation of the dissipation term \mathbf{Q}_α in Eq. (4), we calculate the equation of motion for the lesser green function $\sigma(t) = -i\mathbf{G}^<(t, t)$ in the equal-time limit. Substituting Eq. (A14) from Eq. (A13) and applying the limit condition $t_- \approx t_+$ during similar derivations of Eq. (A21), one obtains

$$\begin{aligned} i\frac{d}{dt}\mathbf{G}^<(t, t) - [\mathbf{h}(t), \mathbf{G}^<(t, t)] &= [\boldsymbol{\Sigma}^R \cdot \mathbf{G}^< + \boldsymbol{\Sigma}^< \cdot \mathbf{G}^A - \mathbf{G}^R \cdot \boldsymbol{\Sigma}^< - \mathbf{G}^< \cdot \boldsymbol{\Sigma}^A](t, t) \\ &= -[\mathbf{G}^R \cdot \boldsymbol{\Sigma}^< + \mathbf{G}^< \cdot \boldsymbol{\Sigma}^A](t, t) + h.c. \end{aligned} \quad (\text{A33})$$

Here, the complex integration has been ignored and the relations in Eq. (A26) are used. By comparing Eq. (A33) with Eq. (3) and using $\sigma(t) = -i\mathbf{G}^<(t, t)$, the dissipation term can be given by

$$\mathbf{Q} = -[\mathbf{G}^R \cdot \boldsymbol{\Sigma}^< + \mathbf{G}^< \cdot \boldsymbol{\Sigma}^A](t, t) + h.c. \quad (\text{A34})$$

Appendix B: Wide-Band Limit approximation for the dissipation term Q_α

By applying the assumptions of the wide-band limit approximation, the advanced self-energy for L and R in Eq. (9) becomes

$$\begin{aligned} \Sigma_{\alpha, mn}^A(t, t') &= i\Theta(t' - t) \sum_{k_\alpha} h_{D\alpha, mk_\alpha}(t) \exp \left\{ i \int_t^{t'} \epsilon_{k_\alpha} + V_\alpha(\bar{t}) d\bar{t} \right\} h_{\alpha D, k_\alpha n}(t') \\ &\simeq \Theta(t' - t) \int_{-\infty}^{\infty} d\epsilon e^{i\epsilon(t' - t)} \left[i \cdot h_{D\alpha, m\bar{k}_\alpha}(t) e \exp \left\{ i \int_t^{t'} V_\alpha(\bar{t}) d\bar{t} \right\} h_{\alpha D, \bar{k}_\alpha n}(t') \right] \\ &= \delta(t' - t) [\Lambda_{\alpha, mn} + i\Gamma_{\alpha, mn}] \end{aligned} \quad (\text{B1})$$

where the matrix in the square bracket in the last line is approximated by the initial $\Sigma_\alpha^A(\epsilon_F)$ at fermi level of the unbiased system¹⁵. $V_\alpha(t)$ is the external potential that is turned on at $t > t_0$, resulting in time-dependent level shifts of $\alpha \in \{L, R\}$. The summation over all single-electron states in the electrodes is replaced by an integration over the entire energy, i.e. $\sum_{k_\alpha} \rightarrow \int_{-\infty}^{\infty} d\epsilon$. The retarded/advanced self-energies are $\Sigma_\alpha^{R,A}(t, t') = [\Lambda_{\alpha, mn} \mp i\Gamma_{\alpha, mn}] \delta(t' - t)$.

The lesser self-energy in Eq. (10) is

$$\begin{aligned}
\Sigma_{\alpha,mn}^<(t,t') &= \sum_{k_\alpha} h_{D\alpha,mk_\alpha}(t) G_{\alpha,k_\alpha}^< h_{\alpha D,k_\alpha m}(t') \\
&= \sum_{k_\alpha} h_{D\alpha,mk_\alpha}(t) h_{\alpha D,k_\alpha m}(t') \left[i \cdot f_\alpha(\epsilon_{k_\alpha}) e^{i\epsilon(t'-t)} e^{i \int_t^{t'} V_\alpha(\bar{t}) d\bar{t}} \right] \\
&= \frac{2i}{\pi} \Gamma_{\alpha,mn} e^{i \int_t^{t'} V_\alpha(\bar{t}) d\bar{t}} \int_{-\infty}^{\infty} f_\alpha(\epsilon) e^{i\epsilon(t'-t)} d\epsilon
\end{aligned} \tag{B2}$$

From Eq. (7), the lesser green function can be solved as

$$\mathbf{G}_D^R(t,t') = -i\Theta(t-t') e^{-i \int_0^t [\mathbf{h}_D(\bar{t}) + \sum_\alpha (\mathbf{\Lambda}_\alpha - i\mathbf{\Gamma}_\alpha)] d\bar{t}} e^{-i \int_{t'}^0 [\mathbf{h}_D(\bar{t}) + \sum_\alpha (\mathbf{\Lambda}_\alpha - i\mathbf{\Gamma}_\alpha)] d\bar{t}} \tag{B3}$$

Inserting Eqs. (B1)-(B3) into Eq. (6), the dissipation term for electrodes L and R can be given by

$$\begin{aligned}
\mathbf{Q}_\alpha(t) &= - \int_{-\infty}^{\infty} d\tau [\mathbf{G}_D^<(t,\tau) \mathbf{\Sigma}_\alpha^A(\tau,t) + \mathbf{G}_D^R(t,\tau) \mathbf{\Sigma}_\alpha^<(\tau,t) + H.c.] \\
&= - \int_{-\infty}^{\infty} d\tau [\mathbf{G}_D^R(t,\tau) \mathbf{\Sigma}_\alpha^<(\tau,t) + H.c.] + \{\mathbf{\Gamma}_\alpha, \sigma(t)\} + i[\mathbf{\Lambda}_\alpha, \sigma(t)]
\end{aligned} \tag{B4}$$

Here, the first term of the integration in the second line can be calculated by

$$\begin{aligned}
\mathbf{K}_\alpha(t) &= - \int_{-\infty}^{\infty} d\tau [\mathbf{G}_D^R(t,\tau) \mathbf{\Sigma}_\alpha^<(\tau,t)] \\
&= \frac{-2}{\pi} \int_{-\infty}^0 d\tau e^{-i \int_\tau^t [\mathbf{h}_D(\bar{t}) + \sum_\alpha (\mathbf{\Lambda}_\alpha - i\mathbf{\Gamma}_\alpha) - V_\alpha(\bar{t})] d\bar{t}} \int_{-\infty}^{\infty} f_\alpha(\epsilon) e^{i\epsilon(t-\tau)} d\epsilon \mathbf{\Gamma}_\alpha \\
&\quad + \frac{-2\Theta(t-\tau)}{\pi} \int_0^{\infty} d\tau e^{-i \int_\tau^t [\mathbf{h}_D(\bar{t}) + \sum_\alpha (\mathbf{\Lambda}_\alpha - i\mathbf{\Gamma}_\alpha) - V_\alpha(\bar{t})] d\bar{t}} \int_{-\infty}^{\infty} f_\alpha(\epsilon) e^{i\epsilon(t-\tau)} d\epsilon \mathbf{\Gamma}_\alpha \\
&= \frac{-2i}{\pi} \mathbf{U}_\alpha(t) \int_{-\infty}^{\infty} \frac{f_\alpha(\epsilon) e^{i\epsilon t}}{\epsilon - \mathbf{h}_D(0) - \sum_\alpha (\mathbf{\Lambda}_\alpha - i\mathbf{\Gamma}_\alpha)} d\epsilon \mathbf{\Gamma}_\alpha \\
&\quad - \frac{2i}{\pi} \int_{-\infty}^{\infty} [\mathbf{I} - \mathbf{U}_\alpha(t) e^{i\epsilon t}] \frac{f_\alpha(\epsilon)}{\epsilon - \mathbf{h}_D(t) - \sum_\alpha (\mathbf{\Lambda}_\alpha - i\mathbf{\Gamma}_\alpha) + V_\alpha(t) \mathbf{I}} d\epsilon \mathbf{\Gamma}_\alpha
\end{aligned} \tag{B5}$$

with

$$\mathbf{U}_\alpha(t) = e^{-i \int_0^t [\mathbf{h}_D(\bar{t}) + \sum_\alpha (\mathbf{\Lambda}_\alpha - i\mathbf{\Gamma}_\alpha) - V_\alpha(\bar{t}) \mathbf{I}] d\bar{t}} \tag{B6}$$

Conclusively, the dissipation term now is

$$\mathbf{Q}_\alpha(t) = \mathbf{K}_\alpha(t) + \mathbf{K}_\alpha^\dagger(t) + \{\mathbf{\Gamma}_\alpha, \sigma(t)\} + i[\mathbf{\Lambda}_\alpha, \sigma(t)] \tag{B7}$$

with the definition of $\mathbf{K}_\alpha(t)$ in Eq. (B5).

REFERENCES

- ¹S. J. Rosenthal, J. C. Chang, O. Kovtun, J. R. McBride, I. D. Tomlinson, *Chemistry & Biology* 18, 10 (2011).
- ²S. Jin, and K. Ye, *Biotechnol. Prog.* 23, 32 (2007).
- ³I. L. Medintz, H. Mattoussi, and A. R. Clapp, *Int. J. Nanomed.* 3, 151 (2008).
- ⁴X. Michalet, F. F. Pinaud, L. A. Bentolila, J. M. Tsay, S. Doose, J. J. Li, G. Sundaresan, A. M. Wu, S. S. Gambhir, and S. Weiss, *Science* 307, 538 (2005).
- ⁵X. Gao, Y. Cui, R. M. Levenson, L. W. K. Chung, and S. Nie, *Nat. Biotech.* 22, 969 (2004).
- ⁶T. Pons, and H. Mattoussi, *Ann. Biomed. Eng.* 37, 1934 (2009).
- ⁷F. Pinaud, S. Clarke, A. Sittner, and M. Dahan, *Nat. Meth.* 7, 275 (2010).
- ⁸A. M. Derfus, W. C. W. Chan, and S. N. Bhatia, *Adv. Mat.* 16, 961 (2004).
- ⁹G. Ruan, A. Agrawal, A. I. Marcus, and S. Nie, *J. Am. Chem. Soc.* 129, 14759 (2007).
- ¹⁰H. Dong, T. Hou, X. Sun, Y. Li, and S. T. Lee, *Appl. Phys. Lett.* 103, 123115 (2013).
- ¹¹Y. Matsumoto, A. Dutt, G. S. Rodriguez, J. S. Salazar, and M. A. Mijares, *Appl. Phys. Lett.* 106, 171912 (2015)
- ¹²S. M. Lindsay, and M. A. Ratner, *Adv. Mater.* 19, 23 (2007).
- ¹³S. Nazemi, M. Pourfath, E. A. Soleimani, and H. Kosina, *J. App. Phys.* 119, 144302 (2016).
- ¹⁴G. Stefanucci, C.O. Almbladh, *Phys. Rev. B* 69(19), 195318(2004).
- ¹⁵Y. Wang, C. Y. Yam, Th. Frauenheim, G.H. Chen, T.A. Niehaus, *Chemical Physics* 391, 69 (2011).
- ¹⁶X. Zheng, F. Wang, C. Y. Yam, Y. Mo, and G. H. Chen, *Phys. Rev. B* 75, 195127 (2007).
- ¹⁷K. Burke, R. Car, and R. Gebauer, *Phys. Rev. Lett.* 94(14), 146803 (2005).
- ¹⁸M. Koentopp, C. Chang, K. Burke, and R. Car, *J. Phys. Condens. Matter* 20, 083203 (2008).
- ¹⁹C. L. Cheng, J. S. Evans, and T. V. Voorhis, *Phys. Rev. B* 74, 155112 (2006).
- ²⁰J. Evans, O. Vydrov, and T. Van Voorhis, *J. Chem. Phys.* 131, 034106 (2009).
- ²¹N. Garcia-Castello, S. Illera, J. D. Prades, S. Ossicini, A. Cirera, and R. Guerra, *Nanoscale* 7, 12564 (2015).
- ²²J. M. Soler, E. Artacho, J. D. Gale, A. Garcia, J. Junquera, P. Ordejon and D. Sanchez-Portal, *J. Phys.: Condens. Matter* 14, 2745 (2002).

- ²³P. Ordejon, E. Artacho and J. M. Soler, Phys. Rev. B: Condens. Matter 53, R10441 (1996).
- ²⁴E. Runge and E. K. U. Gross, Phys. Rev. Lett. 52, 997 (1984).
- ²⁵I. L. Ho, T. H. Chou, and Y. C. Chang, Comput. Phys. Commun. 185, 1383 (2014).
- ²⁶J. C. Cuevas, and E. Scheer, *Molecular Electronics: An Introduction to Theory and Experiment*, World Scientific, 2010
- ²⁷R. Tuovinen, E. Perfetto, G. Stefanucci, and R. van Leeuwen, Phys. Rev. B 89, 085131 (2014).
- ²⁸A. P. Jauho, N. S. Wingreen, and Y. Meir, Phys. Rev. B 50, 5528 (1994).
- ²⁹S. Yokojima, G. Chen, R. Xu, and Y. Yan, Chem. Phys. Lett., 369(3), 495 (2003).
- ³⁰M. P. Lopez-Sancho, J. M. Lopez-Sancho, and J. Rubio, J. Phys. F: Met. Phys. 14, 1205 (1984); 15, 851 (1985).
- ³¹W. M. C. Foulkes and R. Haydock, Phys. Rev. B 39 12520 (1989).
- ³²M. Elstner, D. Porezag, G. Jungnickel, J. Elsner, M. Haugk, Th. Frauenheim, S. Suhai, and G. Seifert, Phys. Rev. B 58 7260 (1998).
- ³³S. Datta, *Quantum Transport: Atom to Transistor*, New York, Cambridge University Press (2005).
- ³⁴H. Grabert, and M. H. Devoret, *Single Charge Tunneling: Coulomb Blockade Phenomena In Nanostructures*, New York, Springer Science & Business Media (1992).
- ³⁵J. A. Melsen, U. Hanke, H. O. Muller, and K. A. Chao, Phys. Rev. B 55 (1997), 10638-10642.
- ³⁶I. L. Ho, D. S. Chung, M. T. Lee, C. S. Wu, Y. C. Chang, and C. D. Chen, J. Appl. Phys. 111 (2012), 064501.
- ³⁷preparing
- ³⁸W. M. Haynes, *CRC Handbook of Chemistry and Physics*, 96th Edition (2015).
- ³⁹D. M. Ceperley and B. J. Alder, Phys. Rev. Lett. 45, 566 (1980).
- ⁴⁰J. P. Perdew and A. Zunger, Phys. Rev. B: Condens. Matter 23, 5048 (1981).
- ⁴¹M. C. Payne, M. P. Teter, D. C. Allan, T. A. Arias and J. D. Joannopoulos, Rev. Mod. Phys. 64, 1045 (1992).
- ⁴²L. S. Wang, Phys. Chem. Chem. Phys. 12, 8694 (2010).
- ⁴³C. G. Sanchez, E. P. M. Leiva, and W. Schmickler, Electrochem. Commun. 5(7), 584 (2003).
- ⁴⁴C. Sevik, and C. Bulutay, J Mater. Sci. 42, 6555 (2007).

- ⁴⁵G. Conibeer, M. A. Green, D. Konig, I. Perez-Wurfl, S. Huang, X. Hao, D. Di, L. Shi, S. Shrestha, B. PuthenVeetil, Y. So, B. Zhang and Z. Wan, *Prog. Photovoltaics: Res. Appl.* 19, 813 (2011).
- ⁴⁶G. Seguini, S. Schamm-Chardon, P. Pellegrino and M. Perego, *Appl. Phys. Lett.* 99, 082107 (2011).
- ⁴⁷K. Seino, F. Bechstedt and P. Kroll, *Phys. Rev. B: Condens. Matter* 82, 085320 (2010).
- ⁴⁸K. Seino, F. Bechstedt and P. Kroll, *Phys. Rev. B: Condens. Matter* 86, 075312 (2012).
- ⁴⁹R. Guerra, E. Degoli and S. Ossicini, *Phys. Rev. B: Condens. Matter* 80, 155332 (2009).
- ⁵⁰M. Mavros, D. A. Micha and D. S. Kilin, *J. Phys. Chem. C* 115, 19529 (2011).